Research Article

A study of structural and dielectric properties of Ba^{2+} doped $CH_3NH_3PbI_3$ crystals

Rasanjali Jayathissa[1] · Clement A. Burns[1]

Received: 29 November 2019 / Accepted: 1 February 2020 / Published online: 6 February 2020

Abstract
An understanding of the effects of doping in lead perovskites may allow for improved solar cell performance or reduction in toxicity of the materials used. Ba^{2+} doped $CH_3NH_3PbI_3$ ($CH_3NH_3Pb_{1-x}Ba_xI_3$ with x = 1%, 5% and 10%) are successfully synthesized by cooling down a concentrated aqueous solution containing HI, CH_3NH_2 and metal acetates and their properties are investigated using x-ray diffraction, differential scanning calorimetry, and impedance spectroscopy (IS). No new structures are formed upon doping with Ba^{2+} ions, however the lattice expands. The IS measurements show a strong increase in the conductivity and dielectric constants of the doped crystals. The conductivity arises mainly from vacancy mediated iodide ion (I^-) migration and the increase in ionic conductivity with dopants is ascribed to increased defect formation due to lattice distortion. In addition, the bulk dielectric constant increases with increasing Ba^{2+} dopant. The increase in the dielectric constant is consistent with ordering of CH_3NH_3 dipoles resulting from distortions of the Ba sites in the lattice. The temperature dependence of the dielectric constants is attributed to thermal effects on the orientation of CH_3NH_3 molecules.

Keywords Organic inorganic hybrid perovskites · Doping · Defects · Impedance analysis · X-ray diffraction

1 Introduction

Using $CH_3NH_3PbX_3$ (X = Br, I) as a photo-absorber in solar cells was first carried out in 2009 by Kojima et al. [1]. Since then, OILH (organic–inorganic lead halide) perovskite based solar cells have been vigorously investigated for their excellent solar cell performance, which comes from material properties such as high light absorption coefficients [2, 3], high dielectric constants, ultrafast carrier charge separation [4, 5], high carrier mobility, and long carrier diffusion lengths [6–9]. Especially interesting are the inexpensive fabrication costs compared to other PV technologies [10]. The rapid progress towards high solar cell efficiencies (> 23% as of 2018) has been achieved within just a few years [11]. However, toxicity of lead (Pb) is a major concern for its further development. Doping of Pb in $CH_3NH_3PbX_3$ perovskites with nontoxic metals has attracted a lot of attention in the perovskite photovoltaic community because of the possibility of improving solar cell properties while reducing the amount of toxic Pb present. Doping is a potential means of improving stability and solar cell lifetime, so measuring the properties of doped perovskites is a necessary first step.

1.1 Tolerance considerations for doping

Perovskite compounds have a crystal structure which consists of three primary ions with a stoichiometry ABX_3

Electronic supplementary material The online version of this article (https://doi.org/10.1007/s42452-020-2157-x) contains supplementary material, which is available to authorized users.

✉ Rasanjali Jayathissa, rasanjali.jayathissa@wmich.edu; Clement A. Burns, clement.burns@wmich.edu | [1]Department of Physics, Western Michigan University, 1903 W. Michigan Ave, Kalamazoo, MI 49008-5252, USA.

similar to calcium titanate. The A, B and X ions are typically represented by a large metal cation, a smaller metal cation and an anion respectively. In the idealized cubic perovskite structure, the ions are arranged in such a way that the cation A forms a 12-fold cuboctahedra coordination and cation B forms a sixfold octahedral coordination of the anion X [2]. The structural stability is deduced by considering the Goldschmidt tolerance factor (t) and the octahedral factor (μ) given by,

$$t = \frac{R_A + R_X}{\sqrt{2\left(R_B + R_X\right)}} \tag{1}$$

$$\mu = \frac{R_B}{R_X} \tag{2}$$

where R_A, R_B and R_X are radii of cation A, cation B and anion X respectively. The t factor evaluates whether the A cation can fit within the cavity formed by the BX_3 framework and the factor μ assesses the fit of the cation B in the BX_6 octahedron [12, 13]. For example, for halide perovskites (where X = F, Cl, Br, I), t and μ lie in the ranges $0.81 < t < 1.11$ and $0.44 < \mu < 0.90$ [13].

Suitable candidates for doping can be selected considering Eqs. 1 and 2 [10, 12]. In this regard, the non-toxic alkaline-earth metal Ba^{2+} (t = 0.871) is compatible in the $CH_3NH_3PbI_3$ perovskite structure in place of Pb^{2+}. Hence without forming new structures Pb^{2+} can be substituted by Ba^{2+}. Using density functional theory (DFT), it has also been predicted that crystals of $CH_3NH_3BI_3$ with B = Ca, Sr and Ba will form with similar formation energies to that of $CH_3NH_3PbI_3$ but with an increased bandgap resulting in worse optical absorption in the visible and infrared [14]. However, partial replacement of Pb with Sr showed a decrease in the bandgap [15]. Ba doping has been shown to deteriorate the photovoltaic performance in $CH_3NH_3PbI_3$ solar cells, but with less effect than in Sr doped cells [16], and 1–5% Ba doping resulted in improved photovoltaic performance in thin film solar cells [17, 18]. Studies where Pb is partially replaced with Ba are relevant to dopant effects on thin films solar cell properties. For this paper Ba doped $CH_3NH_3PbI_3$ polycrystals ($CH_3NH_3Pb_{1-x}Ba_xI_3$ with x = 1%, 5% and 10%) were synthesized, and structural, calorimetric, conductivity, and dielectric properties are investigated. Our work studies how Ba dopants affect material properties (in 3D crystals) such as structure, ionic conductivity, and the dielectric constant, and it provides further insights on dopants and their effects on material properties.

2 Materials and methods

2.1 Crystal preparation

Lead acetate trihydrate ($Pb(CH_3CO_2)_2{\cdot}3H_2O$) (≥ 99%, CAS 6080-56-4), barium acetate ($Ba(CH_3CO_2)_2$) (99%, CAS 543-80-6), methylamine (CH_2NH_2) (40 wt% (aq.), CAS 74-89-5) and hydro iodide acid (HI) (57 wt% (aq.), CAS 10034-85-2) were purchased from Alfa Aesar and used as received.

Polycrystalline $CH_3NH_3Pb_{1-x}Ba_xI_3$ was synthesized by slightly modifying the method described by Poglitsch and Weber [19]. The undoped sample (x = 0) was prepared by dissolving 0.625 g of Pb-acetate in 2.5 ml of concentrated aqueous HI in a Pyrex round bottom flask heated in a silicon oil bath using a magnetic stirrer. The molar ratio of Pb-acetate to Ba-acetate was chosen to be 1 − x: x (x = 0.01, 0.05 and 0.1) for Ba doped samples. The obtained solution was pale yellow in color. In a separate container, another 0.5 ml of HI was mixed with 0.1664 ml of aqueous methylamine in an ice bath and added dropwise to the first solution. A black precipitate formed upon slow (~ 5 day) cooling from 110 to 50 °C, and was filtered and dried overnight at 70 °C in a vacuum oven.

2.2 X-ray diffraction

2θ x-ray diffraction scans on powdered samples deposited on a single crystal Si zero background holder were obtained using a PANalytical Empyrean X-ray Diffraction System using Cu $K_{\alpha 1}$ (1.54060 Å) x-rays. Measurements were taken in vacuum. Measurements in air over several days resulted in the degradation of the sample as shown by color change (from black to yellow) and the diffraction data. No changes over the measurement time were observed for the samples in vacuum.

2.3 Differential scanning calorimetry

DSC measurements were performed on ~ 7 mg samples using a TA Instruments DSC Q100 calorimeter at a rate of temperature change of 10 °C min^{-1} from 35 to 100 °C under nitrogen gas flow.

2.4 Impedance spectroscopy (IS)

For the IS measurements, thin cylindrical pellets were prepared by pressing powdered crystals using a hydraulic press. To reduce the effect of strain, the pellets were annealed at 70 °C for about an hour. The pellet was sandwiched between two copper (Cu) electrodes and the impedance data was collected using a QuadTech 1920

precision LCR meter. Dark measurements of capacitance (C) and complex impedance (*Z*) were carried out in the frequency range from 20 Hz to 1 MHz with a 1 V AC signal under 0 V DC bias for the temperature range of 25–65 °C. Nyquist plots were created and the equivalent RC parallel circuits were identified and used to calculate bulk conductivity and dielectric constant.

3 Results

The ideal powder diffraction patterns for the pristine sample at room temperature (294 K) were simulated using Rietveld modeling with High Score Plus software to index the PXRD peaks (Fig. 1). The simulation for the pristine sample was obtained using the available theoretical structural data [20] (space group symmetry, unit cell dimensions, and relative coordinates of atoms in unit cell, atomic site occupancies, and atomic thermal displacement parameters). This simulated result was used to identify the hkl values for the peaks with the experimental sample and to confirm the room temperature tetragonal phase (I4/mcm space group).

Then, for all the samples, PXRD profiles were fitted using the available default profile fitting function with the High Score Plus software to obtain more precise peak information about position, intensity, width and shape of the diffraction peaks in the profile. Si references peaks were aligned, and angles were taken from reference profile ICDD 00-027-1402.

The PXRD profiles for the Ba doped samples and a standard Si (NIST) powder are shown in Fig. 2a.

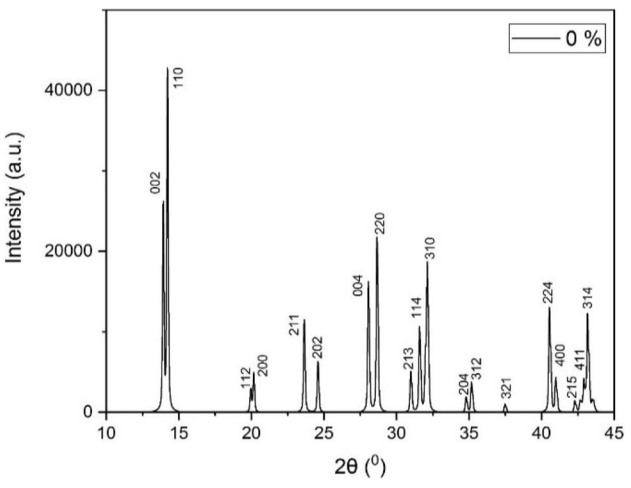

Fig. 1 Simulated powder XRD pattern for pristine sample with labeled peaks (the Cu $K_{\alpha 1}$ wavelength is 1.54060 Å, Tetragonal I4/mcm space group at temperature 294 K)

Si peaks from different runs are aligned, and with increasing Ba%, a peak shift towards lower 2θ angles is observed as shown for the (110) peak in Fig. 2b. The shoulder peak is ascribed to the (002). The variations in lattice parameters are calculated using these peaks (Table 1).

As given in Fig. 3, Vegard's law, which states the change of the lattice constant is proportional to the concentration of the dopant for a crystal whose lattice reacts as an elastic medium, was used to verify the dopant amounts [21]. The lattice parameters for pristine $CH_3NH_3PbI_3$ [19] and $CH_3NH_3BaI_3$ [22] were used to find the relationship between lattice constant and Ba%. The Ba^{2+} doped $CH_3NH_3PbI_3$ samples exhibit tetragonal to cubic transition peaks at ~ 57 °C and ~ 56 °C for heating and cooling curves respectively as confirmed by the DSC plots (Online Resource).

Nyquist plots of impedance at different frequencies show single distorted semicircular arcs whose radii become smaller as the temperature increases (Fig. 4). The real axis intercept of these semicircular arcs was obtained by extrapolating the curves to estimate the sample resistance (R). The Apex frequency (f_p) of the Nyquist semi-circle is given by the relation

$$2\pi f_p RC = 1 \tag{3}$$

where f_p is a fundamental parameter which is independent of the geometry, known as the relaxation frequency of the material [23]. Using this relation, the bulk capacitance (C) can be determined and the bulk dielectric constant (ε_b) of the material can be found by,

$$C = \varepsilon_0 \varepsilon_b \frac{A}{d} \tag{4}$$

where ε_0 is the permittivity of free space, A is the area of the pellet and d is the thickness.

Furthermore, as shown in Fig. 5, the dark conductivity of the Ba^{2+} doped $CH_3NH_3PbI_3$ samples increases by over two orders of magnitude with increasing Ba content. The bulk dielectric constant of doped $CH_3NH_3PbI_3$ samples increases with increasing Ba content as shown in Fig. 6.

Furthermore, the frequency and temperature dependence of dielectric constant of Ba doped $CH_3NH_3PbI_3$ can be analyzed as follows. The dielectric constant (ε) can be written as a complex number,

$$\varepsilon = \varepsilon' - j\varepsilon'' \tag{5}$$

where ε' and ε'' are the real and imaginary part of the dielectric constant. The ε' represents the dispersion, which is the dependence of ε of the material on the frequency of an applied field, and the ε'' represents the loss characteristic of the dielectric response. The ratio between, ε' and ε'' is known as the loss tangent,

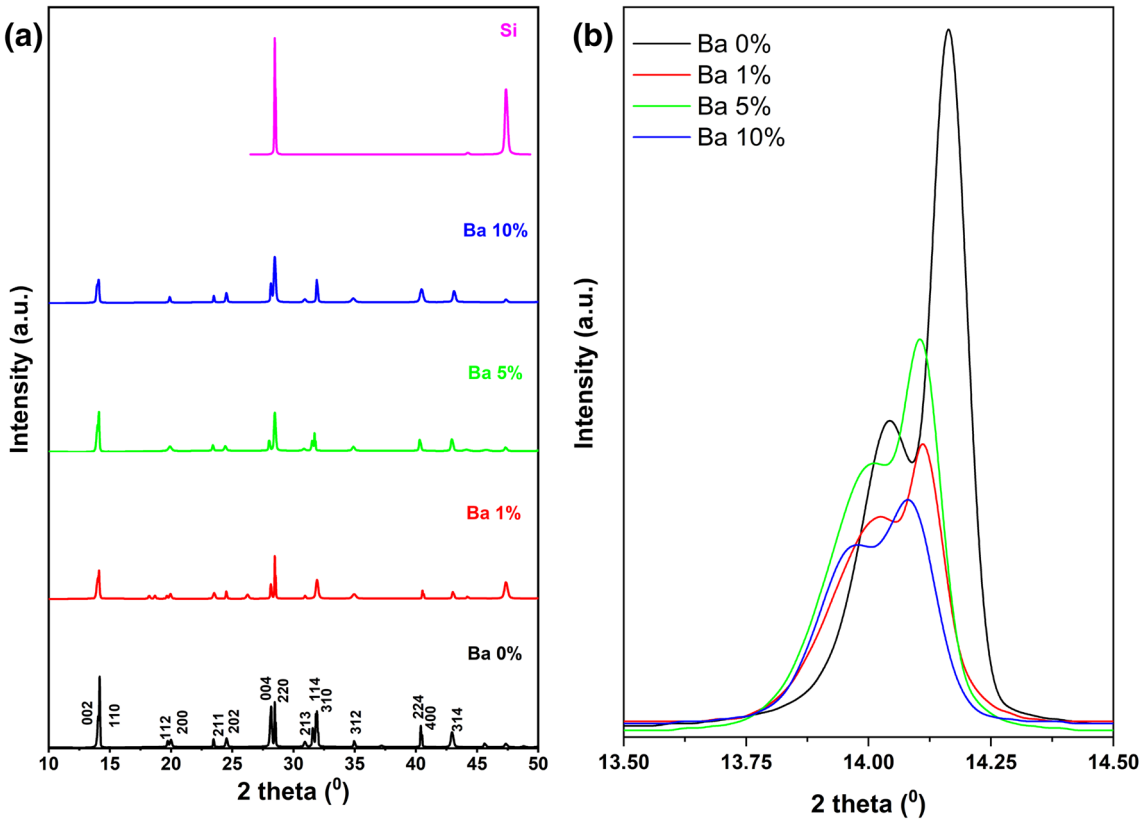

Fig. 2 **a** PXRD profiles with indexed peaks for Ba^{2+} doped $CH_3NH_3PbI_3$ crystals with Si peaks aligned together. **b** Peak shift of (110) peak for Ba^{2+} doped $CH_3NH_3PbI_3$ crystals. The shoulder peak is the (002)

Table 1 Variation of unit cell parameters a, c with Ba%

Ba%	a (Å)	c (Å)
0	8.8471 ± 0.0001	12.6218 ± 0.0002
1	8.8702 ± 0.0001	12.6298 ± 0.0002
5	8.8740 ± 0.0001	12.6388 ± 0.0002
10	8.9085 ± 0.0001	12.7138 ± 0.0002

$$\tan\delta = \frac{\varepsilon''}{\varepsilon'} \tag{6}$$

and, ε' and ε'' can be expressed as,

$$\varepsilon' = \frac{d}{2\pi f A \varepsilon_0}\left[\frac{-Z''}{Z'^2 + Z''^2}\right] \tag{7}$$

$$\varepsilon'' = \frac{d}{2\pi f A \varepsilon_0}\left[\frac{Z'}{Z'^2 + Z''^2}\right] \tag{8}$$

where d is the thickness of the pellet, A is the surface area of the electrode, and ε_0 and f are the vacuum permittivity and the frequency respectively [24] Z′ and Z″ are the real and imaginary part of the measured impedance. The

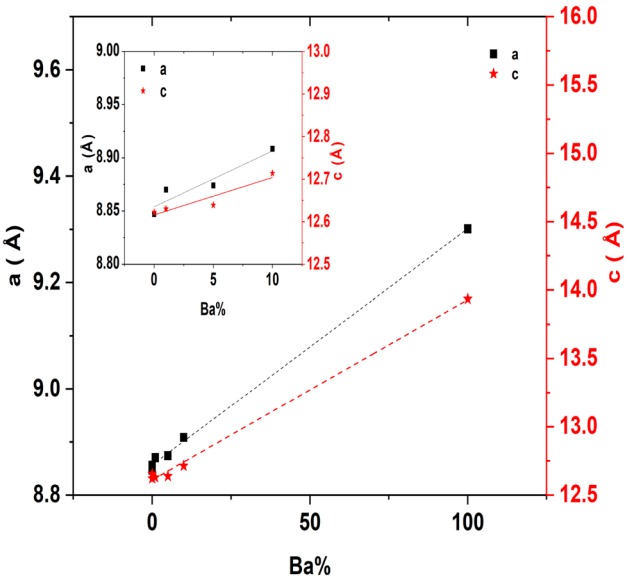

Fig. 3 The variation of the lattice constants a and c with Ba%. The calculated values are compared with the linear trend of Vegard's law (inset) (the error bars are 0.01% of data)

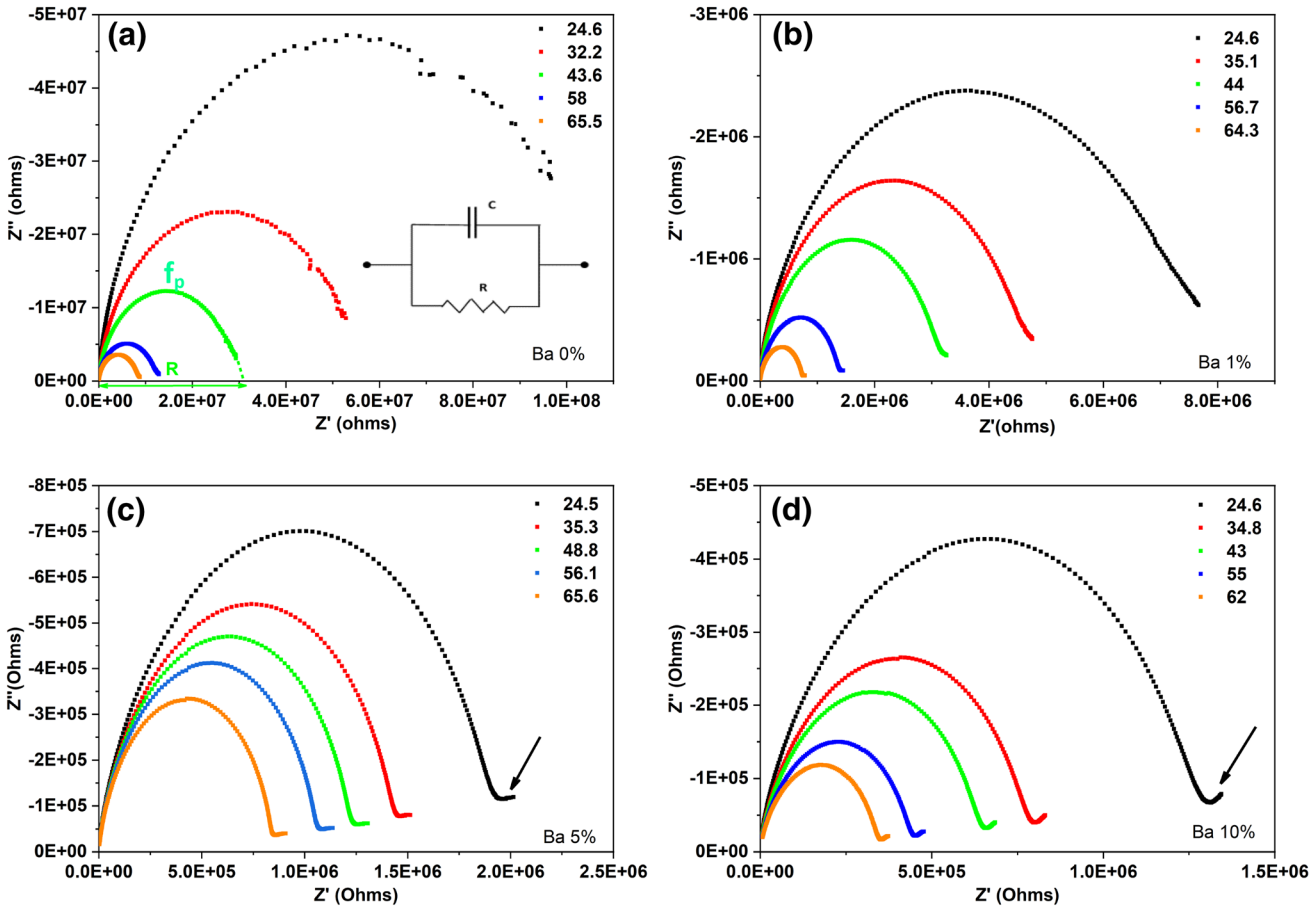

Fig. 4 Temperature dependence of the Nyquist plots for $CH_3NH_3Pb_{1-x}Ba_xI_3$ pellets sandwiched between two Cu electrodes. **a** x=0, **b** x=0.01, **c** x=0.05, **d** x=0.10. The extrapolated arc R is shown in figure **a** and the arrows in figures **c** and **d** show the beginning of the grain boundary arc (error bars are on the order of graph point size). The inset in figure **a** shows the equivalent RC circuit for Nyquist plots with a single semicircular arc and f_p represents the apex frequency position. Temperatures are given in °C

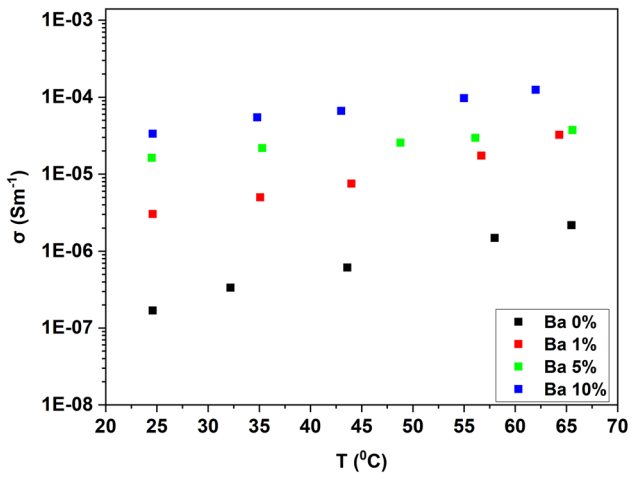

Fig. 5 Temperature and composition dependence of dark conductivity of Ba^{2+} doped $CH_3NH_3PbI_3$ pellets (error bars are on the order of graph point size)

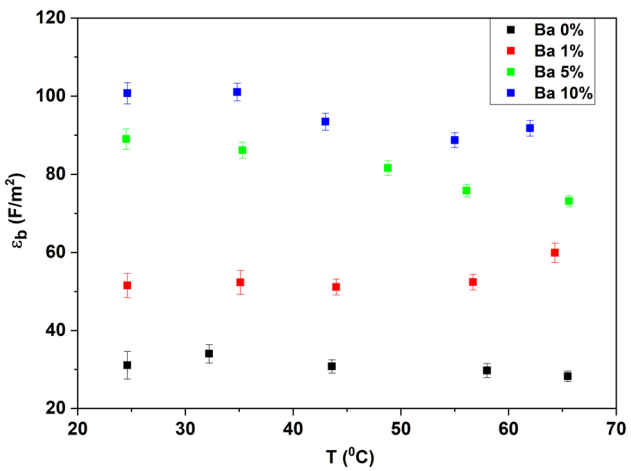

Fig. 6 Variation of bulk dielectric constant calculated using the apex frequency (f_p) of the Nyquist plots with Ba% and temperature of Ba^{2+} doped $CH_3NH_3PbI_3$ pellets

frequency and temperature dependence of the real part of the dielectric constant (ε') for different Ba% is shown in Fig. 7 while Fig. 8 shows the imaginary part of the dielectric constant. At low frequencies the dielectric function increases with temperature and Ba content and the dielectric loss function shows 1/f dependency near low frequencies.

Moreover, the loss tangent ($\tan\delta$) plotted against frequency for different temperatures shows high values at low frequencies and the peak value shifts toward high frequency (shown by an arrow) as the temperature is increased (Fig. 9).

4 Discussion

As shown in Fig. 2a, no new peaks arise upon doping implying that the tetragonal structure of the undoped material is preserved, and no impurity phases form with measurable concentrations. The lattice expands with increasing Ba% due to the replacement of Pb^{2+} (1.19 Å) with Ba^{2+} (1.35 Å) [25]. As shown in Fig. 3, the experimental lattice constants are consistent with the amounts in the solution used for synthesis. As confirmed by the DSC results, the phase transition temperature for the undoped sample is in good agreement with previously reported transition temperatures [26] and for the doped samples this temperature remains essentially the same. No additional peaks in the DSC profile within the used temperature range also implies that no other structural transitions occur.

According to Nyquist plots given in Fig. 4, the bulk resistance decreases with the increase in temperature and thus the bulk conductivity increases with temperature. These arcs emerge at high frequencies which corresponds to a bulk effect [23, 27]. A low frequency arc starts to emerge which corresponds to grain boundary effects [23], as the Ba increases in the sample from 5 to 10%. Even though the grain boundary effect is not fully detectable within the range of the frequencies studied, it can be concluded that the high number of dopants can modify the grain boundary behavior. As shown in Fig. 5, there is a significant increase of the dark conductivity with increasing Ba content. The dark conductivity in $CH_3NH_3PbI_3$ was found to be mostly ionic in previous studies [28] and is thought to arise from point-defect mediated ion migration of $CH_3NH_3^+$ [29, 30] and I^- [31–33]. The activation energy for migrations of I^- (0.58 eV) is smaller than $CH_3NH_3^+$ (0.84 eV) and Pb^{2+} (2.3 eV) from first principle calculations [34]. Also, the I^- on the edge of PbI_6^{4-} octahedra have a

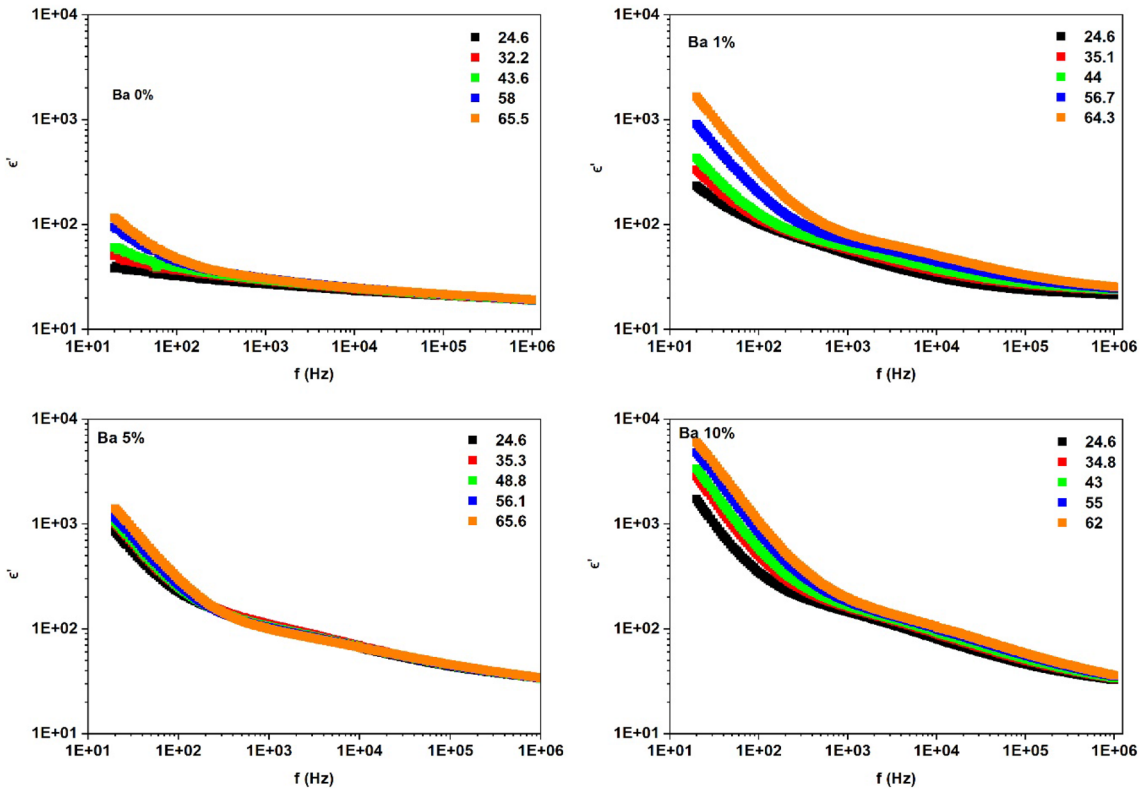

Fig. 7 Temperature dependence of real part of dielectric constant for Ba^{2+} doped $CH_3NH_3PbI_3$ pellets (temperatures are given in °C and error bars are on the order of graph point size)

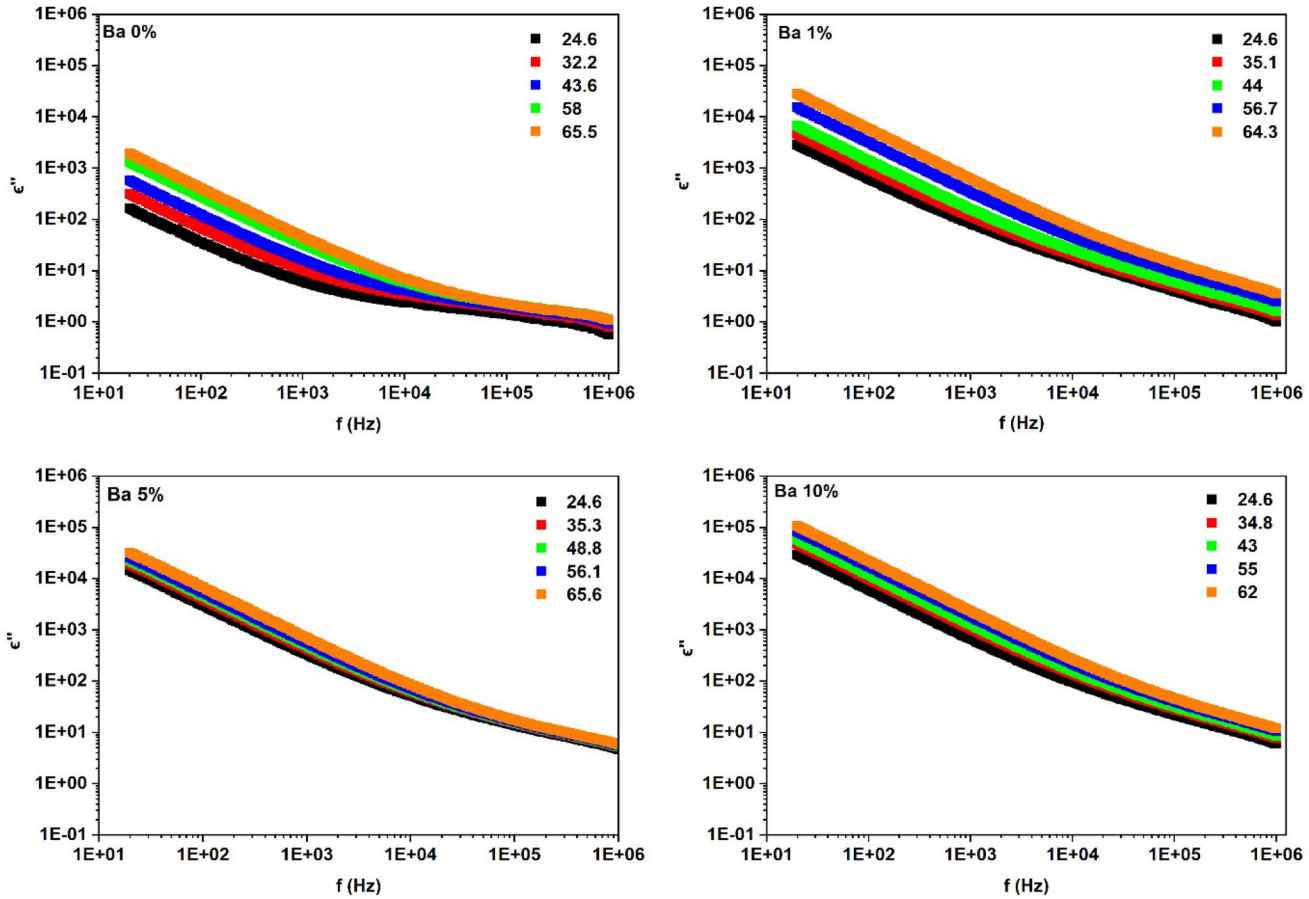

Fig. 8 Temperature dependence of imaginary part of dielectric constant for Ba^{2+} doped $CH_3NH_3PbI_3$ pellets (temperatures are given in °C and error bars are on the order of graph point size)

shorter distance to the nearest I^- vacancy (~4.46 Å) than Pb^{2+} (~6.28 Å) ions, again favoring I^-conductivity [35]. Since the Ba^{2+} is isovalent to Pb^{2+}, the observed increase in ionic conductivity is not related to isovalent doping. When the Pb^{2+} is replaced by the larger Ba^{2+} ion, atoms locally rearrange their positions resulting in a tensile strain near the Ba site and leaving the neighboring Pb site under compression. We propose that strain increases the defect concentration thereby increasing the ionic conductivity. The Gibbs free energy for accommodating vacancies into the lattice, includes the loss of bond energy with a vacancy but the gain of configurational entropy. The number of vacancies in a lattice can be approximated by,

$$n \approx exp\left(\frac{-H}{mkT}\right) \tag{9}$$

where n is the number of vacancies, H is defect formation enthalpy, k is Boltzmann constant, T is absolute temperature and m is an integer (= 1 for point defects, = 2 for Frenkel defects). The defect formation within the lattice will be enhanced by lowering the defect formation energy. We suggest that in the Ba doped lattice, the defect formation energy is lower and thereby the number of vacancies present is higher than in the pristine lattice. An increase in vacancies will result in an increase in I^- conductivity. The enhancement of defect formation is related to the lattice distortion by the Ba ions. In ionic and heteropolar crystals like $CH_3NH_3PbI_3$, the interactions are influenced by the Madelung electrostatic potential [36]. The electrostatic interaction ($u^{coul}(r)$) per ion pair has the form,

$$u^{coul}(r) = -\alpha\frac{e^2}{r} \tag{10}$$

where α is the Madelung constant, which depends only on the crystal structure and the coordination number, i.e., the number of nearest neighbors (of opposite charge), r is the nearest neighbor distance and e is the electron charge [37]. As given in Fig. 10a, in the undoped lattice, iodine in the Pb–I plane is predominantly affected by interaction with Pb ions, whereas, in $CH_3NH_3Pb_{1-x}Ba_xI_3$ there are different interactions due to neighboring Ba and Pb

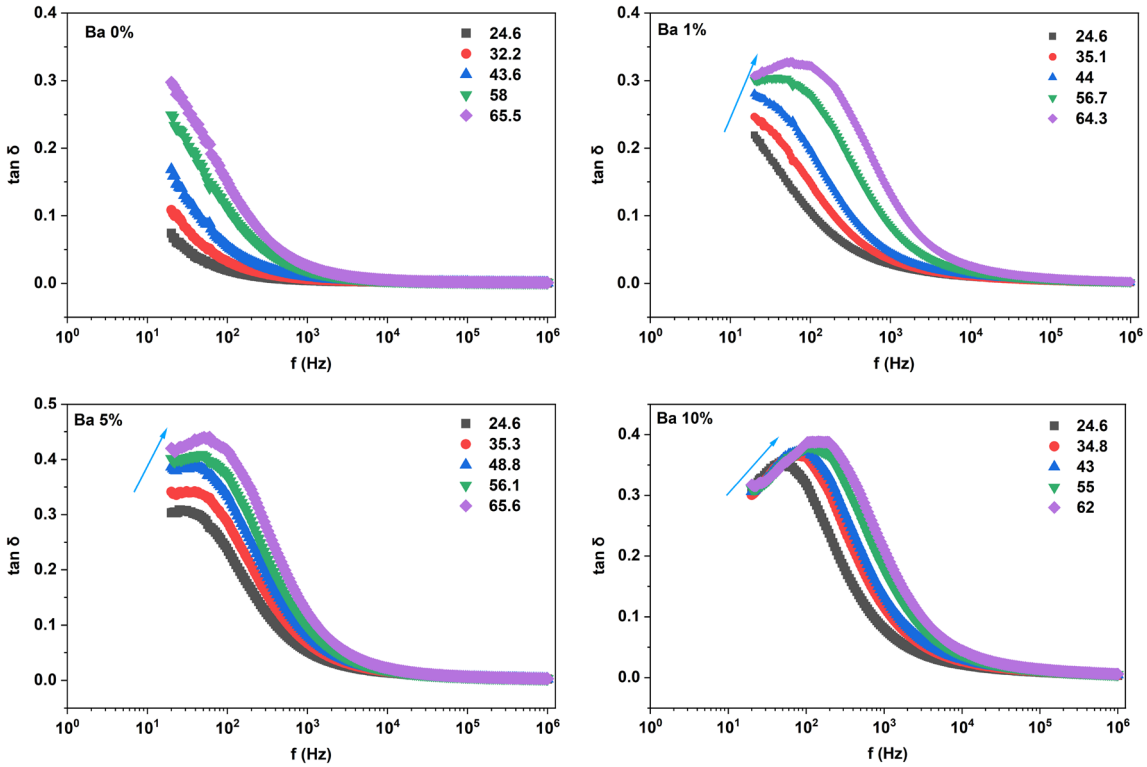

Fig. 9 Temperature and frequency dependence of loss tangent for Ba^{2+} doped CH_3NH_3PbI3 pellets (temperatures are given in °C and error bars are on the order of graph point size)

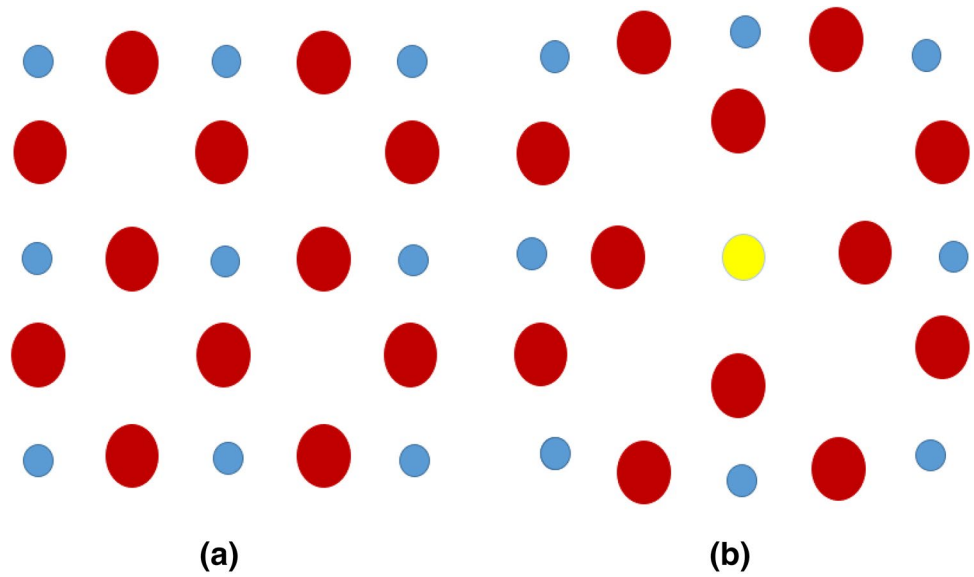

Fig. 10 Schematic atomic arrangement in the Pb–I plane in **a** $CH_3NH_3PbI_3$ and **b** $CH_3NH_3Pb_{1-x}Ba_xI_3$ lattice. Red, blue and yellow circles represent I, Pb and Ba atoms respectively (here, for simplicity, the octahedral tilting of the tetragonal structure is not shown)

ions (Fig. 10b). Since the crystal structure remains the same upon addition of the Ba dopants, the coordination number for I in both lattices is same. But the Ba–I bond length (3.23 Å) is larger than that of Pb–I (3.11 Å) [14]. Consequently, the absolute value for the Madelung potential is smaller for iodine in the Ba doped lattice. This smaller interaction may enhance displacement of an iodine atom from the lattice site into a nearby interstitial site, forming an iodine vacancy and interstitial (Frenkel pair). The interstitial can be in close proximity to the vacancy due to the spatial availability near the Ba site. In the case of the undoped lattice such Frenkel pairs will cost more energy

to form. Hence Ba sites may introduce extra vacancies in the lattice by Frenkel defect formation and so enhance the ionic conductivity for increasing Ba amounts.

There is an increase in dark conductivity by an order of magnitude from 0 to 5% (10^{-6}–10^{-5} S m^{-1}) Ba^{2+} doping and then as higher dopant concentration is approached (10%) the conductivity starts to saturate (Fig. 4). This can be due to formation of Ba clusters at high concentrations which may saturate the number of defects at Ba sites and the clusters can also act as scatters for the ionic motion thereby decreasing the ionic conductivity. Moreover, as seen in the Fig. 5, the conductivity increases with temperature. The increased thermal vibrations make it easier for an iodine atom to move to nearby vacancy and enhance the ionic motion.

Moreover, as shown in Fig. 6, there is an increasing bulk dielectric constant with increasing Ba content. The dielectric constant (ε) of a material is defined as

$$\varepsilon = \varepsilon_0 + \frac{P}{E} \tag{11}$$

where *P* and *E* are the magnitudes of polarization $\bar{P}$ and applied electric field $\bar{E}$ vectors. Note that $\bar{P}$ is the contribution from both induced and permanent dipoles in the material. In $CH_3NH_3PbI_3$, the $CH_3NH_3^+$ ion has a permanent electric dipole moment; thus, changing the orientation of this ion will contribute to the dielectric properties [38–40] Specially, within the frequency range where the bulk properties were determined (MHz regime), the polarization response is principally the contribution from $CH_3NH_3^+$ rotation and its associated dipole moment along the C–N bond axis [41]. Near room temperature the entropy associated with $CH_3NH_3^+$ orientation is high and upon lowering the temperature, the entropy of $CH_3NH_3^+$ dipole orientation decreases, reflecting an increase in the dielectric constant [42]. In that low temperature orthorhombic phase $CH_3NH_3^+$ are well-oriented to maximize the hydrogen bonding with I in PbI_6 octahedral [43]. In contrast, in the tetragonal phase CH_3NH_3 molecules are randomly oriented and show no orientational correlation resulting in high orientational disorder [42]. Considering the above facts, reduction of the orientational disorder of CH_3NH_3 molecules in the tetragonal lattice will enhance the dielectric constant. To explain the observed behavior of dielectric constant with Ba incorporation, we suggest that the distortion from the Ba sites causes the orientation of CH_3NH_3 molecules to be ordered to some extent and thereby increases the dielectric constant. Since the orientation of CH_3NH_3 molecules depends on the hydrogen bonds it forms with iodides in octahedron [44], displacement of I due to lattice distortion may introduce a preferred orientation of CH_3NH_3 molecules. In the literature, similar behavior in dielectric constant with dopant was reported for Fe^{2+} doped $CH_3NH_3PbI_3$ films and the behavior was attributed to the creation of larger grains during the crystallization due to the high residual stress cause by the Fe^{2+} dopants [45]. In contrast, the increase in the dielectric constant with increased Ba content, improves exciton separation, promoting free charges which is beneficial for solar cell performance, while reducing Pb content. Also, there is a variation of the dielectric constant with temperature (Fig. 6). This can be due to thermal effects on the orientational polarization. As the molecules receive more thermal energy the random motion becomes greater, and molecules align less closely with each other reducing orientational polarization and hence the dielectric constant is lowered. This effect is observed experimentally up to ~ 55 °C as shown in Fig. 6. After that the trend shows a discontinuity likely due to the tetragonal to cubic phase transition shown in the DSC data. From the DSC curve the transition temperature was calculated to be 57 °C. During the phase change, the structural change will affect the orientation of the dipoles and hence the dielectric constant will change.

At low frequency there is a clear increase in the dielectric function (Fig. 7) which agrees with the previously published reports for pristine samples [31, 46–48]. This change is attributed to slow ionic migration of I^- [49]. From the same plots it is also evident that ε' increases with increasing Ba concentration. This agrees with the assumption we made earlier about more defect formation with increasing Ba% in the sample, which leads to enhancement of I^- motion. Also, at low frequencies ε' increases with temperature whereas at high frequencies (~ MHz) the rate of increase is reduced. In the high frequency region, the polarization response is mainly from reorientation of $CH_3NH_3^+$ ions with a permanent dipole and the increase in ε' can be ascribed to the CH_3NH_3 ordering with Ba incorporation as previously described. As shown in Fig. 8, the dielectric loss (ε'') shows 1/f dependence below 10 kHz, a phenomenon known as 'Jonscher's law' which indicates ionic conductivity of the material [48, 50].

In the loss tangent plot (Fig. 9) a peak appears in the low frequency region which gradually shifts towards high frequency with increasing Ba concentration and temperature. In addition, with more barium the value and the peak frequency of tan δ increases. The peak behavior in the loss tangent plot (Fig. 9) can be attributed to increased formation of defects due to lattice distortion caused by the Ba. Similar loss peak behavior was reported in the literature for Mg^{2+} doped barium zirconate titanate (BZT) ceramic [51]. As mentioned earlier, at low frequencies the dielectric response comes from I^- motion. So, this loss can be attributed to conduction loss of the iodide ions. As more I^- ions are present with the increased doping, they can cause more collisions during ion conduction and thereby

increase the value of loss tangent at a given temperature. However, we do not have an explanation of the loss tangent peak value shifting towards high frequency (Fig. 9). Similar behavior for $CH_3NH_3PbI_3$ thin films has been reported [52] but also not explained.

5 Conclusions

In conclusion, nontoxic Ba doped $CH_3NH_3PbI_3$ polycrystals ($CH_3NH_3Pb_{1-x}Ba_xI_3$ with x = 1, 5 and 10) were successfully synthesized. The room temperature tetragonal structure of pristine $CH_3NH_3PbI_3$ perovskite is preserved upon Ba^{2+} doping at 1, 5 and 10% dopant concentrations but the lattice expands with increasing Ba% which is ascribed to the replacement of Pb^{2+} with Ba^{2+} which has a larger ionic radius (1.35 Å) than Pb^{2+} (1.19 Å). For the dopant concentrations studied, there is no effect on the tetragonal to cubic phase transition temperature. The dark I^- ion conductivity of prepared perovskite samples increases with increasing Ba content. The conductivity increase with Ba concentration is ascribed to an increase in I^- conductivity from additional vacancies. The bulk dielectric constant also increases with increasing Ba which promotes formation of free charge carriers, beneficial for solar cell performance while reducing the amount of Pb. This increase is correlated to the ordering of CH_3NH_3 dipoles and the distortions of the Ba sites in the lattice. Additionally, a temperature dependence of the dielectric constants is observed and attributed to thermal effects on orientation polarization of CH_3NH_3 molecules.

Acknowledgements We would like to thank Dr. Gellert Mezei, Dr. Basil Mohammed and Tad Carter for the initial guidance on crystal preparation, and Dr. Pnina Ari-Gur, Department of Mechanical and Aerospace Engineering, Western Michigan University for use of the PANalytical XRD facility which was funded by NSF MRI Award 1626276. Additional funds for the research were provided by the Western Michigan University FRACAA fund.

Compliance with ethical standards

Conflict of interest We declare that we have no conflicts of interest.

References

1. Kojima A, Teshima K, Shirai Y, Miyasaka T (2009) Organometal halide perovskites as visible-light sensitizers for photovoltaic cells. J Am Chem Soc 131(17):6050–6051
2. Yin WJ, Shi T, Yan Y (2014) Unique properties of halide perovskites as possible origins of the superior solar cell performance. J Adv Mater 26(27):4653–4658
3. Yin WJ, Yang JH, Kang J, Yan Y, Wei SH (2015) Halide perovskite materials for solar cells: a theoretical review. J Mater Chem A 3(17):8926–8942
4. Brivio F, Walker AB, Walsh A (2013) Structural and electronic properties of hybrid perovskites for high-efficiency thin-film photovoltaics from first-principles. APL Mater 1(4):042111
5. Tanaka K, Takahashi T, Ban T, Kondo T, Uchida K, Miura N (2003) Comparative study on the excitons in lead-halide-based perovskite-type crystals $CH_3NH_3PbBr_3$ $CH_3NH_3PbI_3$. Solid State Commun 127(9–10):19–623
6. Giorgi G, Fujisawa JI, Segawa H, Yamashita K (2013) Small photocarrier effective masses featuring ambipolar transport in methylammonium lead iodide perovskite: a density functional analysis. J Phys Chem Lett 4(24):4213–4216
7. Anaya M, Lozano G, Calvo ME, Míguez H (2017) ABX_3 perovskites for tandem solar cells. Joule 1(4):769–793
8. Wehrenfennig C, Eperon GE, Johnston MB, Snaith HJ, Herz LM (2014) High charge carrier mobilities and lifetimes in organolead trihalide perovskites. J Adv Mater 26(10):1584–1589
9. Buin A, Pietsch P, Xu J, Voznyy O, Ip AH, Comin R, Sargent EH (2014) Materials processing routes to trap-free halide perovskites. Nano Lett 14(11):6281–6286
10. Green MA, Ho-Baillie A, Snaith HJ (2014) The emergence of perovskite solar cells. Nat Photonics 8(7):506
11. NREL Transforming Energy, Best Research-Cell Efficiency Chart (2019). https://www.nrel.gov/pv/cell-efficiency.html. Accessed 06 Oct 2019
12. Goldschmidt VM (1926) The laws of crystal chemistry. Nat Sci 14(21):477–485
13. Li C, Lu X, Ding W, Feng L, Gao Y, Guo Z (2008) Formability of ABX_3 (X = F, Cl, Br, I) halide perovskites. Acta Crystallogr B Struct Sci 64(6):702–707
14. Pazoki M, Jacobsson TJ, Hagfeldt A, Boschloo G, Edvinsson T (2016) Effect of metal cation replacement on the electronic structure of metal organic halide perovskites: replacement of lead with alkaline-earth metals. Phys Rev B 93(14):144105
15. Shai X, Zuo L, Sun P et al (2017) Efficient planar perovskite solar cells using halide Sr-substituted Pb perovskite. Nano Energy 36:213–222
16. Wu MC, Chen WC, Chan SH, Su WF (2018) The effect of strontium and barium doping on perovskite-structured energy materials for photovoltaic applications. Appl Surf Sci 429:9–15
17. Zhang H, Shang MH, Zheng X, Zeng Z, Chen R, Zhang Y, Zhang J, Zhu Y (2017) Ba^{2+} doped $CH_3NH_3PbI_3$ to tune the energy state and improve the performance of perovskite solar cells. Electrochim Acta 254:165–171
18. Wu MC, Lin TH, Chan SH, Liao YH, Chang YH (2018) Enhanced photovoltaic performance of perovskite solar cells by tuning alkaline earth metal-doped perovskite-structured absorber and metal-doped TiO_2 hole blocking layer. ACS Appl Energy Mater 1(9):4849–4859
19. Poglitsch A, Weber D (1987) Dynamic disorder in methylammoniumtrihalogenoplumbates (II) observed by millimeter-wave spectroscopy. J Chem Phys 87(11):6373–6378
20. Weller MT, Weber OJ, Henry PF, Di Pumpo AM, Hansen TC (2015) Complete structure and cation orientation in the perovskite photovoltaic methylammonium lead iodide between 100 and 352 K. Chem Commun 51(20):4180–4183
21. Leszczyński M, Litwin-Staszewska E, Suski T, Bąk-Misiuk J, Domagała J (1995) Lattice constant of doped semiconductor. Acta Phys Pol A 88(5):837–840
22. Kumar A, Balasubramaniam KR, Kangsabanik J, Alam A (2016) Crystal structure, stability, and optoelectronic properties of the organic-inorganic wide-band-gap perovskite $CH_3NH_3BaI_3$: candidate for transparent conductor applications. Phys Rev B 94(18):180105
23. MacDonald JR, Johnson WB (2005) Fundamentals of impedance spectroscopy. In: Barsoukov E, MacDonald JR (eds) Impedance

spectroscopy: theory, experiment, and applications, 2nd edn. Wiley, Hoboken, NJ, p 15
24. Lanfredi S, Rodrigues ACM (1999) Impedance spectroscopy study of the electrical conductivity and dielectric constant of polycrystalline $LiNbO_3$. J Appl Phys 86(4):2215–2219
25. Database of Ionic Radii. http://abulafia.mt.ic.ac.uk/shannon/ptable.php. Accessed 6 Oct 2019
26. Baikie T, Fang Y, Kadro JM, Schreyer M, Wei F, Mhaisalkar SG, Graetzel M, White TJ (2013) Synthesis and crystal chemistry of the hybrid perovskite (CH_3NH_3) PbI_3 for solid-state sensitised solar cell applications. J Mater Chem A 1(18):5628–5641
27. Fleig J (2002) The grain boundary impedance of random microstructures: numerical simulations and implications for the analysis of experimental data. Solid State Ion 150(1–2):181–193
28. Senocrate A, Moudrakovski I, Kim GY, Yang TY, Gregori G, Grätzel M, Maier J (2017) The nature of ion conduction in methylammonium lead iodide: a multimethod approach. Angew Chem Int 56(27):7755–7759
29. Yuan Y, Chae J, Shao Y, Wang Q, Xiao Z, Centrone A, Huang J (2015) Photovoltaic switching mechanism in lateral structure hybrid perovskite solar cells. Adv Energy Mater 5(15):1500615
30. Contreras L, Idígoras J, Todinova A, Salado M, Kazim S, Ahmad S, Anta JA (2016) Specific cation interactions as the cause of slow dynamics and hysteresis in dye and perovskite solar cells: a small-perturbation study. Phys Chem Chem Phys 18(45):31033–31042
31. Li C, Tscheuschner S, Paulus F, Hopkinson PE, Kießling J, Köhler A, Vaynzof Y, Huettner S (2016) Iodine migration and its effect on hysteresis in perovskite solar cells. J Adv Mater 28(12):2446–2454
32. Yang TY, Gregori G, Pellet N, Grätzel M, Maier J (2015) The significance of ion conduction in a hybrid organic–inorganic lead-iodide-based perovskite photosensitizer. Angew Chem Int 54(27):7905–7910
33. Peng W, Anand B, Liu L, Sampat S, Bearden BE, Malko AV, Chabal YJ (2016) Influence of growth temperature on bulk and surface defects in hybrid lead halide perovskite films. Nanoscale 8(3):1627–1634
34. Eames C, Frost JM, Barnes PR, O'regan BC, Walsh A, Islam MS (2015) Ionic transport in hybrid lead iodide perovskite solar cells. Nat Commun 6:7497
35. Yuan Y, Huang J (2016) Ion migration in organometal trihalide perovskite and its impact on photovoltaic efficiency and stability. Acc Chem Res 49(2):286–293
36. Frost JM, Butler KT, Brivio F, Hendon CH, Van Schilfgaarde M, Walsh A (2014) Atomistic origins of high-performance in hybrid halide perovskite solar cells. Nano Lett 14(5):2584–2590
37. Ashcroft NW, Mermin ND (1976) Solid state physics. Brooks/Cole, Belmont, p 405
38. Filippetti A, Delugas P, Saba MI, Mattoni A (2015) Entropy-suppressed ferroelectricity in hybrid lead-iodide perovskites. J Phys Chem Lett 6(24):4909–4915
39. Fabini DH, Hogan T, Evans HA, Stoumpos CC, Kanatzidis MG, Seshadri R (2016) Dielectric and thermodynamic signatures of low-temperature glassy dynamics in the hybrid perovskites $CH_3NH_3PbI_3$ and $HC(NH_2)_2PbI_3$. J Phys Chem Lett 17(3):376–381
40. Leguy AM, Frost JM, McMahon AP et al (2015) The dynamics of methylammonium ions in hybrid organic–inorganic perovskite solar cells. Nat Commun 6:7124
41. Herz LM (2018) How lattice dynamics moderate the electronic properties of metal-halide perovskites. J Phys Chem Lett 9(23):6853–6863
42. Onoda-Yamamuro N, Matsuo T, Suga H (1992) Dielectric study of $CH_3NH_3PbX_3$ (X = Cl, Br, I). J Phys Chem Solids 53(7):935–939
43. Lee JH, Bristowe NC, Bristowe PD, Cheetham AK (2015) Role of hydrogen-bonding and its interplay with octahedral tilting in $CH_3NH_3PbI_3$. Chem Commun 51(29):6434–6437
44. Lee JH, Lee JH, Kong EH, Jang HM (2016) The nature of hydrogen-bonding interaction in the prototypic hybrid halide perovskite, tetragonal $CH_3NH_3PbI_3$. Sci Rep 6:21687
45. Ippili S, Jella V, Kim J, Hong S, Yoon SG (2018) Enhanced piezoelectric output performance via control of dielectrics in Fe^{2+}-incorporated $MAPbI_3$ perovskite thin films: flexible piezoelectric generators. Nano Energy 49:247–256
46. Juarez-Perez EJ, Sanchez RS, Badia L, Garcia-Belmonte G, Kang YS, Mora-Sero I, Bisquert J (2014) Photoinduced giant dielectric constant in lead halide perovskite solar cells. J Phys Chem Lett 5(13):2390–2394
47. Anusca I, Balčiūnas S, Gemeiner P et al (2017) Dielectric response: answer to many questions in the methylammonium lead halide solar cell absorbers. Adv Energy Mater 7(19):1700600
48. Lin Q, Armin A, Nagiri RCR, Burn PL, Meredith P (2015) Electro-optics of perovskite solar cells. Nat Photonics 9(2):106
49. Beilsten-Edmands J, Eperon GE, Johnson RD, Snaith HJ, Radaelli PJ (2015) Non-ferroelectric nature of the conductance hysteresis in $CH_3NH_3PbI_3$ perovskite-based photovoltaic devices. Appl Phys Lett 106(17):173502
50. Jonscher AK (1978) Analysis of the alternating current properties of ionic conductors. J Mater Sci 13(3):553–562
51. Xu Y, Zhang K, Fu L, Tong T, Cao L et al (2019) Effect of MgO addition on sintering temperature, crystal structure, dielectric and ferroelectric properties of lead-free BZT ceramics. J Mater Sci Mater Electron 30:7582–7589
52. Hoque MNF, Yang M, Li Z, Islam N, Pan X, Zhu K, Fan Z (2016) Polarization and dielectric study of methylammonium lead iodide thin film to reveal its nonferroelectric nature under solar cell operating conditions. ACS Energy Lett 1(1):142–149